Energy 260 (2022) 125183

Contents lists available at ScienceDirect

Energy

journal homepage: www.elsevier.com/locate/energy

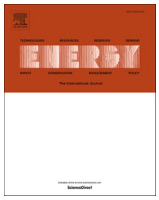

Nitrogen oxide emissions analyses in ammonia/hydrogen/air premixed swirling flames

Syed Mashruk [a,*], Marina Kovaleva [a], Ali Alnasif [a,b], Cheng Tung Chong [c], Akihiro Hayakawa [d], Ekenechukwu C. Okafor [e], Agustin Valera-Medina [a]

[a] College of Physical Sciences and Engineering, Cardiff University, UK
[b] Department of Aeronautical Techniques, Engineering Technical College of Al-Najaf, Al-Furat Al-Awsat Technical University, Najaf, 31001, Iraq
[c] China-UK Low Carbon College, Shanghai Jiao Tong University, Shanghai, China
[d] Institute of Fluid Science, Tohoku University, Sendai, Japan
[e] Faculty of Engineering, Kyushu University, Fukuoka, Japan

ARTICLE INFO

Keywords:
NO_X
Ammonia
Hydrogen
Combustion
Power generation
Chemiluminescence

ABSTRACT

Ammonia/hydrogen fuel blends have gathered interest as a promising solution for the development of a hydrogen economy, with advantages in storage cost or combustion properties compared to pure hydrogen or pure ammonia, respectively. In that pursuit, the present work reports the trends of nitrogen oxide emissions for ammonia/hydrogen blends at atmospheric conditions. NO, NO_2 and N_2O productions/consumptions are approached in detail in combination with unburnt ammonia. All cases are measured in a turbulent, swirl-stabilised flame configuration across hydrogen fuel fractions from 0% to 25% and equivalence ratios from 0.55 to 1.30. A detailed chemistry analysis was conducted using a chemical reactor network (CRN) employing detailed reaction chemistry. The results show that NO and NO_2 emissions peaks around $\Phi = 0.8$, whereas considerable amount of N_2O is generated at very lean conditions, $\Phi \leq 0.65$. Availability of OH radicals and O/H pools in the flames contribute towards fuel NO formation, which in turn produces NO_2 and N_2O. However, very lean conditions lead to lower temperatures that ensure the survival of N_2O. The results identified $\Phi = 1.05$–1.2 as the optimum equivalence ratios for reduced NO_X emissions in ammonia/hydrogen blends, with further understanding of the flame chemistry responsible behind these emissions.

1. Introduction

Since the recent demonstration of ammonia and ammonia/methane combustion in a 50 kW micro gas turbine combustor by Kurata et al. [1], ammonia has seen a surge of renewed interest as an alternative fuel to establish a hydrogen economy, which led to detailed reviews by Valera-Medina et al. [2], Elishav et al. [3], and Kobayashi et al. [4]. Historically, combustion of pure ammonia has faced numerous challenges which have delayed its use as an industrial-scale fuel vector [5]. These challenges include a low heat release rate [4], low laminar burning velocity (maximum ~7 cm/s for NH_3 vs ~37 cm/s for CH_4) [6] high NO emissions under near-stoichiometric conditions attributed to increased fuel-NO [7] and a narrow range of stability [8]. Some solutions that can enhance the flame intensity of ammonia include fuel preheating [1], oxygen enrichment [9], or doping with more reactive fuels like syngas [10], methane [11], hydrogen [12] and both methane and hydrogen [13]. Hydrogen is a particularly promising additive, given its higher heat release rate and combustion intensity. Furthermore, within a combustion system, ammonia can be cracked at relatively low temperatures in-situ to produce hydrogen, as has previously been demonstrated in internal combustion engine systems [14]. However, research has shown that storage and transportation of hydrogen can be both challenging and expensive such that a binary fuel of higher ammonia/lower hydrogen content are a compromise between cost and combustion characteristics, [15].

Recent studies by Pugh et al. [16], Zhang et al. [17], and Franco et al. [18] have explored the product gas trends of ammonia/hydrogen flames in industrially relevant, swirl burner flame configurations. Furthermore, research of ammonia/methane flames in a tangential swirl burner configuration by Valera-Medina et al. [19] found that traditional, injection configurations are not suitable for ammonia-based blends, while other studies found that an approximate 30%/70% blend of H_2/NH_3 or

* Corresponding author.
E-mail address: mashruks@cardiff.ac.uk (S. Mashruk).

https://doi.org/10.1016/j.energy.2022.125183
Received 30 January 2022; Received in revised form 30 June 2022; Accepted 14 August 2022
Available online 18 August 2022

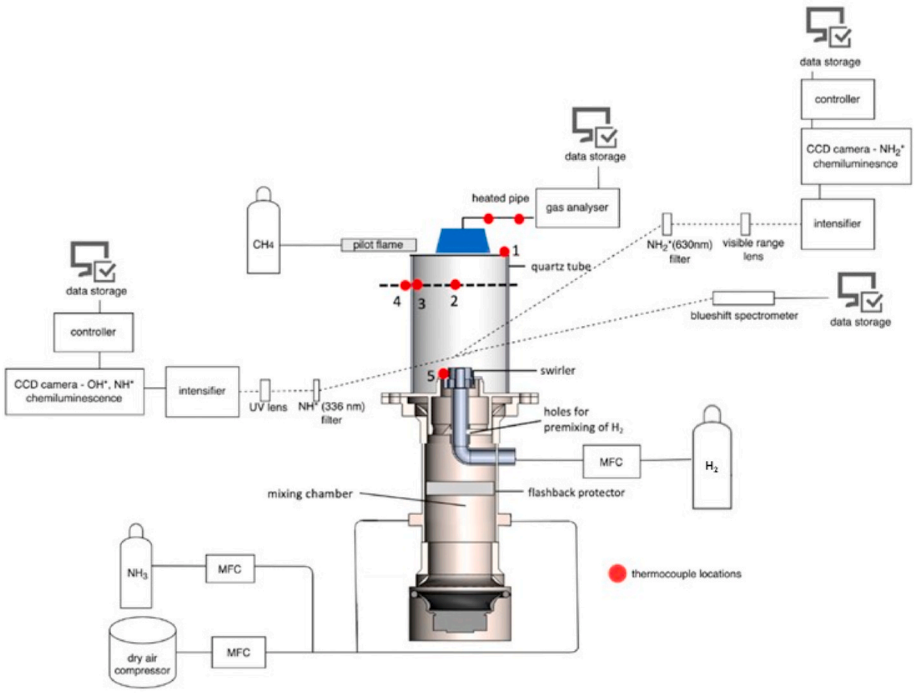

Fig. 1. Tangential combustor with measuring techniques and control systems.

CH_4/NH_3 is beneficial for combustion stability, as both high hydrogen [8] and high ammonia [20] blends can promote instability. Sorrentino et al. [21] showed the applicability of MILD combustion for pure ammonia with good stability and emissions performance when the reactor temperature was above 1300 K. Subsequent study by Ariemma et al. [22] showed that the addition of water in MILD ammonia combustion has the potential to improve both NO_X emissions and stability regions, especially under fuel-lean conditions. Experimental studies in an industrial micro gas turbine system propose the use of two stage rich-lean combustion configuration, for both pure ammonia [23], ammonia/methane blends [24] and more recently, for liquid ammonia [25] combustion. Recent numerical study by Bozo et al. [26] on ammonia/hydrogen rich-quench-lean burners showed comparative efficiency to fossil fuel based power plants. These studies show that the NO emissions of the first (rich) stage should be optimised based on equivalence ratio to achieve low emissions at the outlet. However, other approaches have been suggested to use single stage combustion under very lean conditions [27]. The work successfully achieved stable, ultra-low NO combustion, although emphasising that other NO_X emissions (particularly N_2O) had not been quantified for these blends at the time. However, N_2O must not been overlooked in the evaluation of product gas trends, as N_2O has a 100-year global warming potential (GWP) that is 310 times that of CO_2 [28]. This means that even relatively low levels of N_2O emission can nullify the benefits of using a carbon-free fuel, in this case, ammonia and hydrogen.

Existing literature mentions the production of N_2O under certain conditions. For example, Lee et al. [29] studied numerically the effects of NH_3 addition on H_2/air flames, showing that increasing NH_3 content in lean flames is a driving factor for N_2O production. Okafor et al. [24] also showed the production of N_2O in the lean region of ammonia/-methane flames with high ammonia fraction. A further study of wall temperature influence on swirl flames suggests that lean combustion conditions in combination with low temperatures can also be a driving factor for N_2O production in ammonia/air flames [30]. Despite this, very few studies provide experimental data for the full trends for N_2O and other product gases in H_2/NH_3 flames at industrial conditions, hence providing the motivation for this experimental campaign.

Recently, Ferraroti et al. [31] studied the uncertainty of modelling turbulent ammonia/hydrogen flames in a flameless burner, comparing the experimental data to chemical reactor network (CRN) data and computational fluid dynamics (CFD) model results. This study found that within the examined conditions, discrepancy in NO emissions caused by uncertainty of reaction rate constants of the detailed reaction chemistry model were significantly higher than the uncertainty derived from the numerical models. To tackle this challenge, commendable research efforts have been placed in studying the underlying chemistry of these blends and the establishing reaction mechanisms optimised for ammonia/hydrogen combustion. Experimental studies based on laminar burning velocity of ammonia [9] and ammonia/hydrogen blends [32] have noted NH (leading dominantly to production of HNO) as the key intermediary for the production of NO, with increasing production and consumption of NO from Zeldovich reactions as H_2 concentration increased. For oxygen enriched ammonia/air flames, Mei et al. [9] was also able to show that NH_2 and NH radicals predominantly formed H_iNO (where $i = 0,1,2$) species, leading to contributing to NO formation, while deNOx reactions of NO with NH_x to form N_2O and N_2H_2 acted as major consumption pathways. Furthermore, N_2O doped flames have been studied by Han et al. [35] showing that an increase in N_2O-doping enhances the laminar burning velocity through increased OH production, the main pathway featuring N_2O being its production from NO and consumption to N_2. Finally, in swirling flames, Mashruk et al. [12] showed correlations between N_2O, NO locations with NH_2, while Mei et al. [33] has established a correlation between NO and NH × H for blends of partially cracked ammonia/air. However, the ability of kinetic reaction mechanisms to predict N_2O has not yet been established and further work is necessary to explore the underlying chemistry that drives NOx emission trends in H_2/NH_3 flames.

Therefore, the present work evaluates the production of N_2O, NO, NO_2 and unburnt ammonia in a turbulent, swirl-stabilised flame configuration in ammonia/hydrogen blends. Effects of changing equivalence ratios on emissions productions, spectral profiles, operability and transient profiles are investigated. This is supported by numerical modelling to describe the underlying chemistry coupled with reaction rate diagrams and sensitivity analysis.

Table 1
Experimental matrix.

Parameter	Value	Parameter	Value
Ammonia mol fraction X_{NH3}	0.75, 0.85, 0.95, 1.00	Inlet Temperature	288 K
Thermal Power	8 kW	Inlet Pressure	0.11 MPa
Equivalence Ratio (Φ)	0.55–1.3	Outlet Pressure	0.10 MPa

2. Methodology

2.1. Experimental set-up

An industrial scale tangential swirl burner with optical access and a geometric swirl number of $S_g = 1.05$, shown in Fig. 1, was employed to run different ammonia/hydrogen blends at a wide range of equivalence ratios (Φ) under atmospheric conditions, as shown in Table 1. The burner set-up was detailed elsewhere [34] and only summarised here. The burner was supplied using Bronkhorst mass flow controllers (±0.5% within a range of 15–95% mass flow). Ammonia and air were injected at the mixing chamber, while hydrogen was injected through 6 equispaced holes (1.5 mm diameter), located 4 cm below the burner exit, angled at 45°, directly into the swirler for premixing with ammonia and air. Table 1 shows the various conditions assessed to determine the impact of ammonia mole fraction on NO_X formation, for a wide range of Φ. The details of the data acquisition process and numerical simulation input requirements are illustrated in Fig. 2. The ammonia fraction in the binary fuel of ammonia/hydrogen, X_{NH3}, was defined by Eq. (1),

$$X_{NH3} = \frac{[NH_3]}{[NH_3] + [H_2]} \quad (1)$$

where [Y] represents mole fraction of species Y.

Time-averaged flame images were recorded with two intensified cameras (LaVision Imager *intense*) running simultaneously, fitted with different bandpass filters chosen to capture NH* (336 nm; $A^3\Pi$–$X^2\Sigma^-$ system [35]) and NH_2* (630 nm; single peak of the NH_2 α band [36]) excited radicals. LaVision Davis v10 was used to gather 500 frames for each data point, which were then temporally averaged, and

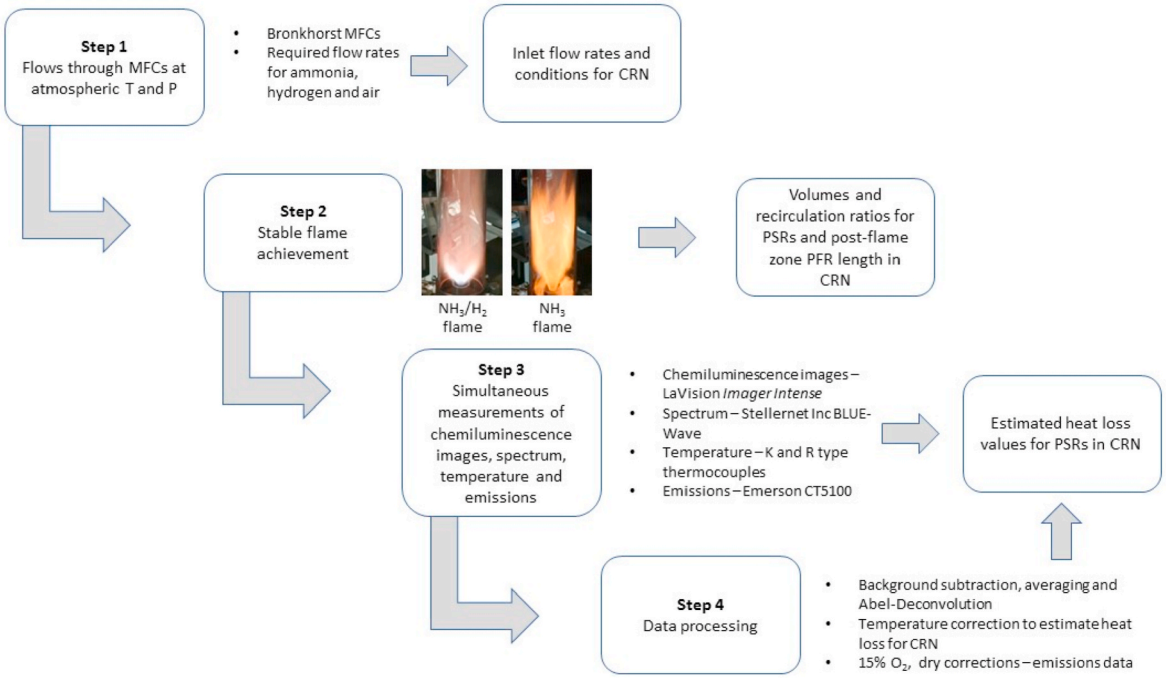

Fig. 2. Step-by-step experimental methodology and inputs for numerical simulation.

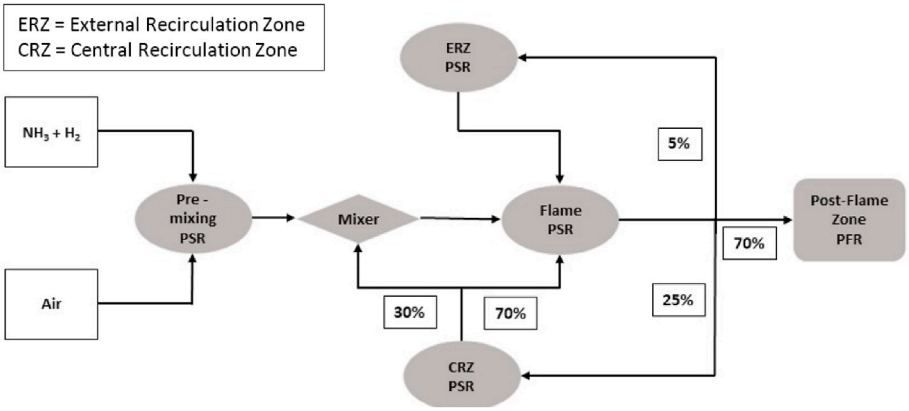

Fig. 3. Chemical reactor network (CRN).

post-processed using a bespoke MatLab script [37] designed to conduct Abel Deconvolution following a 3 × 3 pixel median filter. Colourmaps of the chemiluminescence images have been normalized to the maximum intensity of each image to display the changes in species distributions for each flame.

A UV/visible-capable optical fiber head (Stellernet Inc DLENS with F600 fiber optic cable) was installed 3 cm above the burner's exit and 10 cm away from its central axis. The other end of the optical fiber was connected to a UV/visible-capable spectrometer (Stellernet Inc BLUE-Wave) featuring a 100-mm focal length and a 25-μm wide entry slit. The spectrometer was equipped with a 600-grooves/mm grating and a Si-CCD detector (Sony ILX511b) featuring 2048 effective pixels of size 14 × 200 μm^2, yielding a spectral resolution of 0.5 nm. The detector's exposure time was set to 1 s and 20 scans were averaged to improve the signal-to-noise ratio (SNR). The Y-axis of the spectrometer was calibrated using a standard light source (SL1 Tungsten Halogen).

Temperature profiles were obtained via K and R type thermocouples feeding a data logger with a frequency of 1 Hz. Thermocouple data were taken for 120 s for each point and averaged. The thermocouples were calibrated showing an average error of 3% of reading. The acquired temperature data were corrected as per [38] to account for the convective and radiative heat transfer of the thermocouples with their surroundings, as well as conductive heat transfer between the thermocouple bead and the connecting thermocouple wires. These corrected temperature data for all the test points at location 2, Fig. 1 are provided in the supplementary material, Table S.2 and plotted against Φ in Fig. S.3. Recorded temperatures for all blends peaked around stoichiometry and dropped more on the lean side, compared to the rich conditions. Exhaust emissions (NO, N_2O, NO_2, NH_3, O_2 and H_2O) were measured using a bespoke quantum cascade laser analyzer (Emerson CT5100) operating at 463 K with a sampling frequency of 1 Hz (±1%, 0.999 linearity). An isokinetic funnel with an intake diameter of 30 mm was fixed at 50 mm above the quartz confinement's exit to capture homogeneous samples from the exhaust for selected operating conditions. All the emissions data reported here were recorded and averaged over a period of 120 s. All the emissions data presented here are normalized to 15% O_2 [39].

2.2. Chemical kinetic modelling

A chemical reactor network (CRN) model, Fig. 3, developed elsewhere [12] was adapted to simulate the chemistry of the experimental flames of Table 1. Inlets were used to provide fuel and air flows as well as the inlet conditions from experimental conditions set in Table 1, with four perfectly stirred reactors (PSR) to model the pre-mixing, flame (FZ), central recirculation (CRZ) and external recirculation zone (ERZ). The recirculation strength was determined by previous experimental campaigns that employed comparable industrial scale swirl burners [12]. The outlet from the flame zone fed a Plug Flow Reactor (PFR) with one dimensional length of 15 cm to simulate reactions in the post-flame zone. The background physics and rationale in the development of this network are detailed in Ref. [37] and summarised in the supplementary material, Section 1. The model was configured with a representative combustor geometry, and averaged residence times were estimated from empirical flow data. Heat losses for PSRs were calculated from the corrected thermocouple data and was fixed for all simulated cases with initial values compared to empirical results at a representative condition ($X_{NH3} = 0.75$ and $\Phi = 1.00$) to give favourable agreement with sampled concentrations. All flows/conditions were then changed in an equivalent way to experiments, with no adjustment to other variables. It should be emphasized that the system developed was primarily used for qualitative analysis of the changing flame chemistry using the observed trends. The model employed the reaction mechanism developed by Stagni et al. for NH_3–H_2-air mixtures [40], with 31 chemical species and 203 reactions. This mechanism has shown good performance for NH_3/H_2/air blends in recent studies [41].

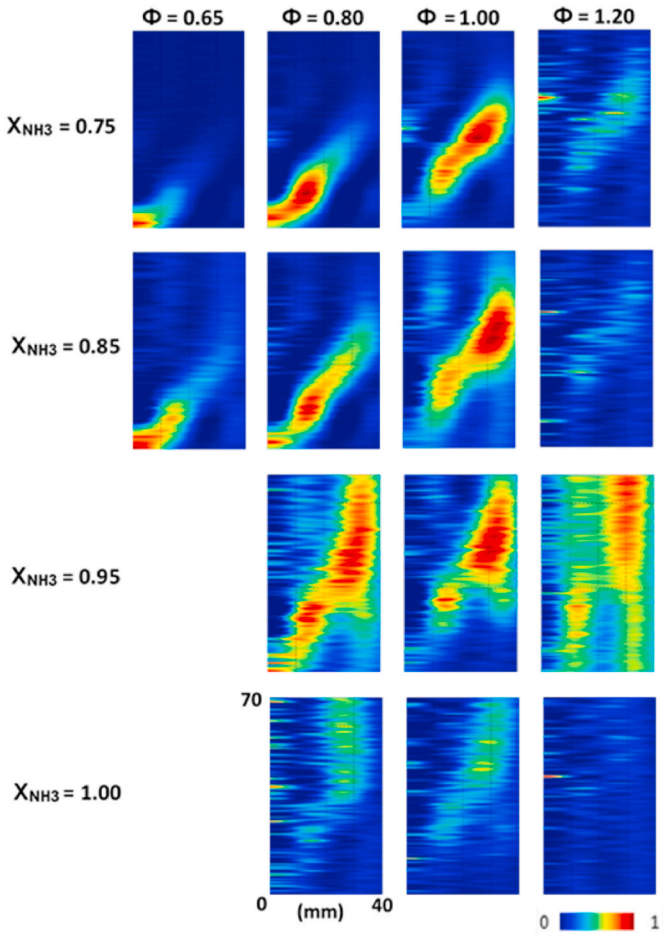

Fig. 4. Abel transformed NH* chemiluminescence images for changing X_{NH3} and Φ. Colourmap normalized to image dataset max.

The final emissions from the simulation were collected at the endpoint of the Post-Flame Zone PFR. To evaluate the contribution of elementary reactions to the formation and consumption of N_2O, absolute rate of production (ROP) values were used for flame zone as 0-D PSR was used to model the flame zone and integrated values of the production rate, I_R, were evaluated for PFZ, as defined in Eq. (2),

$$I_R = \int_0^L \dot{\omega}_{R,i}\, dx \tag{2}$$

where $\dot{\omega}_{R,i}$ is the rate of production of the species, i, through the reaction, R. The length of the integration domain, L, was set to 15 cm, as per the defined length of PFZ.

3. Results and discussions

Figs. 4 and 5 illustrate Abel-Deconvoluted NH* and NH_2* excited radicals, respectively, when changing X_{NH3} and Φ. Note that the origin corresponds to the burner centreline. Increase in flame brush thickness is observed with increasing X_{NH3}, while with increasing Φ, flame lifts off gradually due to the balance between flame speed and inlet flow speed. Due to ammonia's narrow flammability limit [13], pure ammonia could not be ignited below 0.8 equivalence ratio. Measured NH* intensities found to be significantly lower than NH_2* across all flames which is also observed in the acquired chemiluminescence spectra by the spectrometer, Fig. 6. Fig. 6 (a) and (b) show chemiluminescence spectrums for constant $X_{NH3} = 0.75$ and $\Phi = 0.65$, respectively. Even though the proportionality between ground state species and electronically excited species is complicated due to various effects such as quenching and

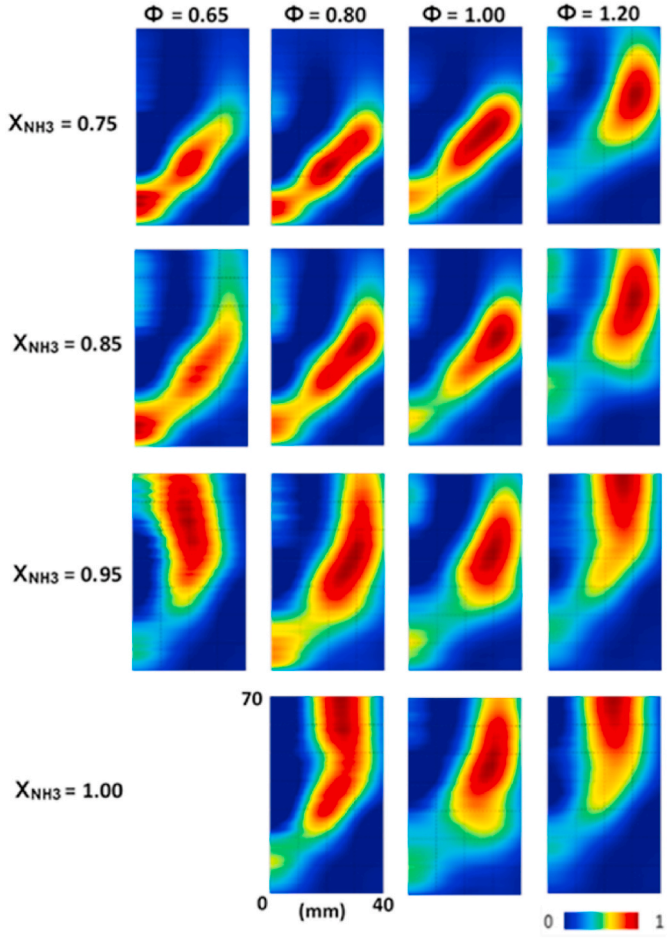

Fig. 5. Abel transformed NH_2* chemiluminescence images for changing X_{NH3} and Φ. Colourmap normalized to image dataset max.

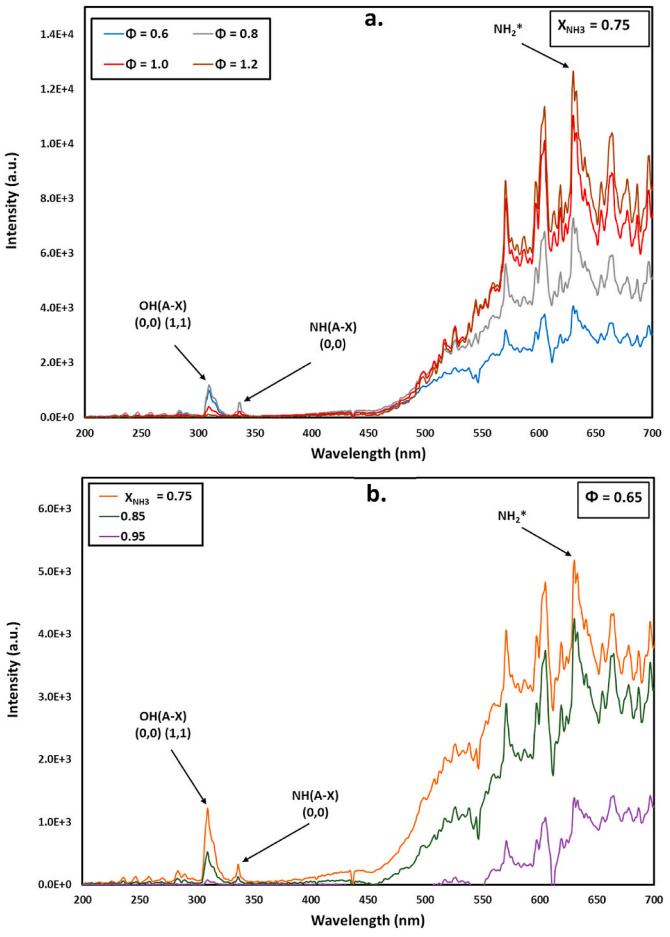

Fig. 6. Chemiluminescence spectrum of 8 kW NH_3/H_2 flames at (a) X_{NH3} = 0.75 and changing Φ, and (b) Φ = 0.65 and changing X_{NH3}.

radiation losses, previous work [42] has assumed proportionality between ground state and electronically excited species in NH_3 disassociation processes. In this study, a similar positive correlation between ground state and emitting species has been applied, thereby more emitting radicals suggest increased ground state population [43–46].

3.1. NH_3 oxidation

The oxidation process of NH_3 starts by reacting with OH radicals to produce NH_2. NH_2 then further reduced to NH by reacting with H, O and OH radicals. NH_2 and NH convert to HNO by reacting with O and OH radicals, respectively. HNO is the main source of NO production at the flame zone. Some of this NO converts to N_2O through the reaction NH + NO ↔ N_2O + H. Most of this N_2O produced in the flame zone convert to N_2 by reacting with H radicals. Unburnt NH_3 emissions measured at the exhaust are plotted in Fig. 7 which also shows the prediction by the CRN at X_{NH3} = 0.75 (blue solid line). Unburnt NH_3 emissions were observed at Φ < 0.60 due to flame instabilities and at rich conditions due to unavailability to oxidise caused by the reduced oxygen content. Emissions between this range are properly captured by the reaction mechanism employed. However, the CRN predictions do not capture NH_3 emissions at very lean conditions and overpredict them at very rich conditions which is in line with recent findings by Manna et al. [47] who investigated the dynamic regime shift at low-intermediate temperature regions (900–1350 K), corresponding to the very lean and rich conditions, a point of interest for further development of more accurate reaction mechanisms.

Fig. 8 displays the normalized sensitivity coefficients for overall NH_3

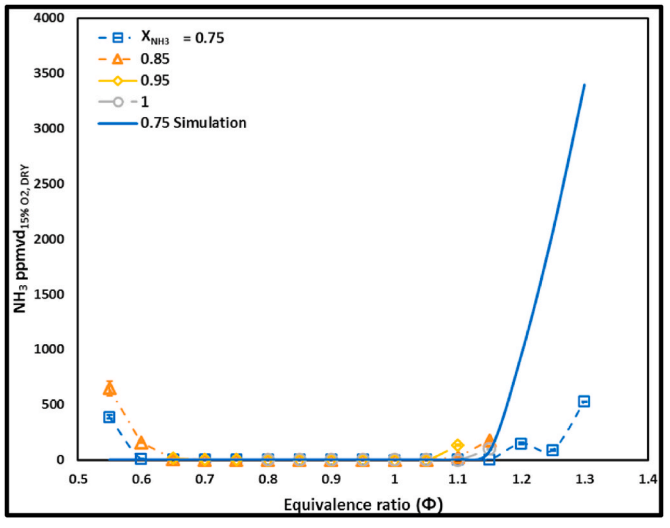

Fig. 7. Sampled NH_3 emissions for changing X_{NH3} and Φ. Markers show experimental results, and the solid line shows simulation prediction.

concentrations at the flame zone while Fig. 9 (a) and (b) show the absolute ROP of [NH_3] at the flame and post-flame zones, respectively, at X_{NH3} = 0.75 and changing Φ. Note that for all the ROP analyses done in this study, ROPs for Φ = 0.6 and 1.0 were increased by an order of magnitude for comparison purposes. From the ROP graphs, the most

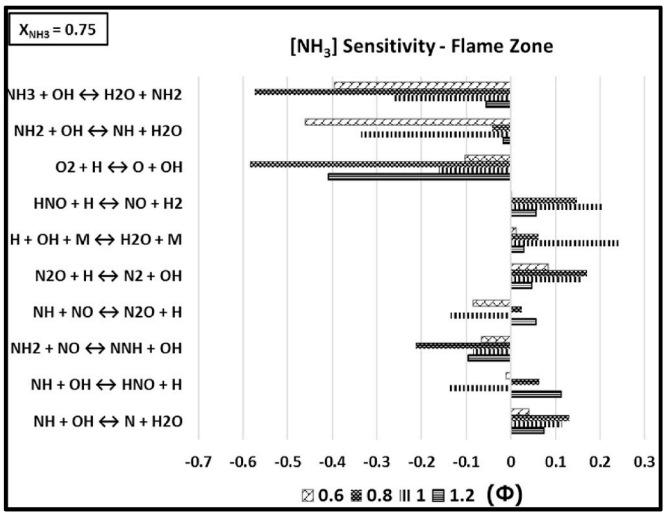

Fig. 8. Normalized sensitivity coefficients of [NH_3] at the flame zone for X_{NH3} = 0.75 and changing Φ.

important reaction for NH_3 oxidation is $NH_3 + OH \leftrightarrow H_2O + NH_2$ (R1). Therefore, any reactions that increase OH radical's availability show negative sensitivity for [NH_3] while the reactions where OH is being consumed show positive sensitivity, Fig. 8. However, the reaction involving N_2O and H radical shows positive sensitivity even though OH radical is being produced. This is due to the fact that the reaction diminishes the availability of H radicals which is vital for OH production through the reaction $O_2 + H \leftrightarrow O + OH$ (R2). Interestingly, reaction R1 has its highest absolute ROP values at Φ = 0.8, followed by Φ = 1.2, 1.0 and 0.6 for both flame zones and post-flame zones. This can be attributed to the sensitivity of the reaction R2 at these equivalence ratios, Fig. 8, which follows the exactly similar trend. It was showed in our previous study [48] that reaction R2 is the main source of OH productions in ammonia/hydrogen/air flames. The other significant source of NH_3 oxidation is when NH_3 reacts with H radicals to produce molecular H_2 and NH_2 radicals. This reaction shows its highest ROP at the rich condition due to the availability of H radicals. These results are in line with NH_2* intensities observed in Fig. 6(a), where increasing NH_2* production increases with Φ. However, NH* production decreases at rich conditions, Fig. 4, due to reduced availability of OH, H and O radicals. Recombination reactions to produce ammonia display very low ROP, confirming NH_3 emissions captured at rich conditions are mainly unburnt ammonia due to reduced availability of oxidising agents.

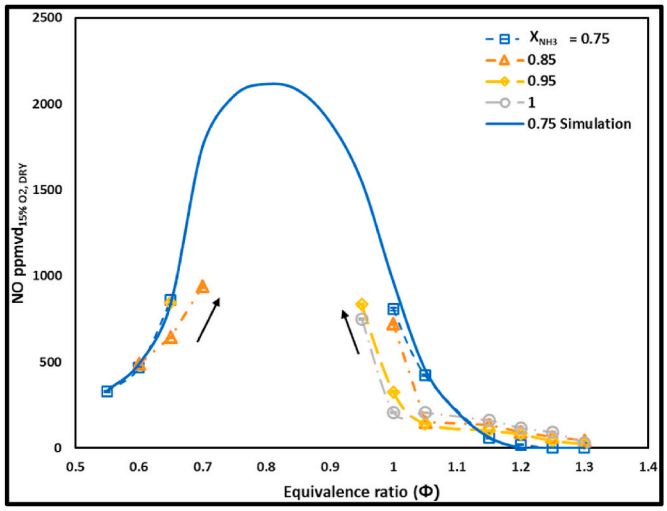

Fig. 10. Sampled NO emissions for changing X_{NH3} and Φ. Markers show experimental results and the solid line shows simulation prediction.

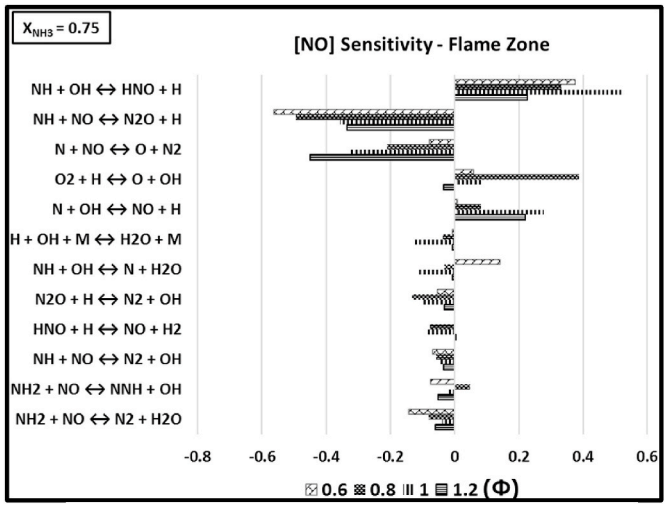

Fig. 11. Normalized sensitivity coefficients of [NO] at the flame zone for X_{NH3} = 0.75 and changing Φ.

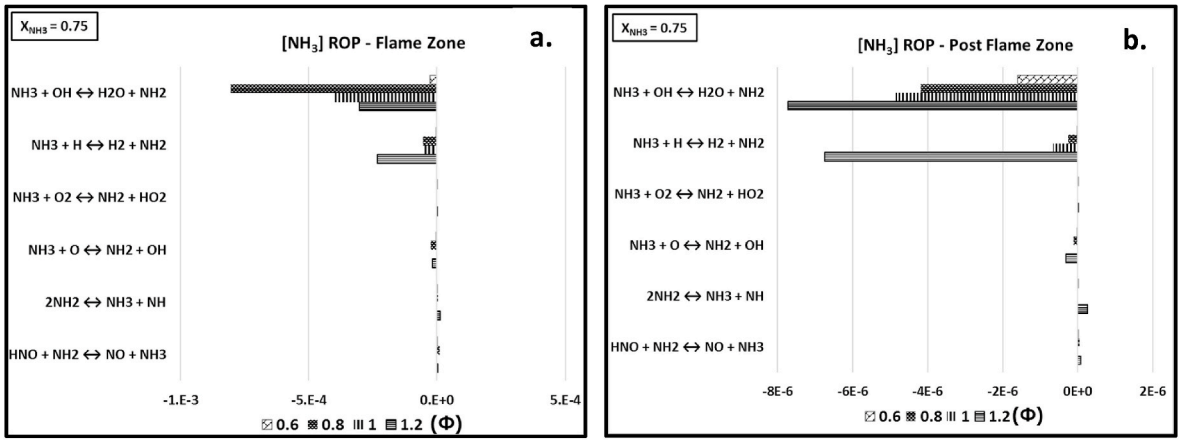

Fig. 9. Absolute and integrated ROPs of [NH_3] at the (a) flame zone [Unit – mole/cm^3-sec], and (b) post-flame zone [Unit – mole/cm^2-sec], respectively for X_{NH3} = 0.75 and changing Φ.

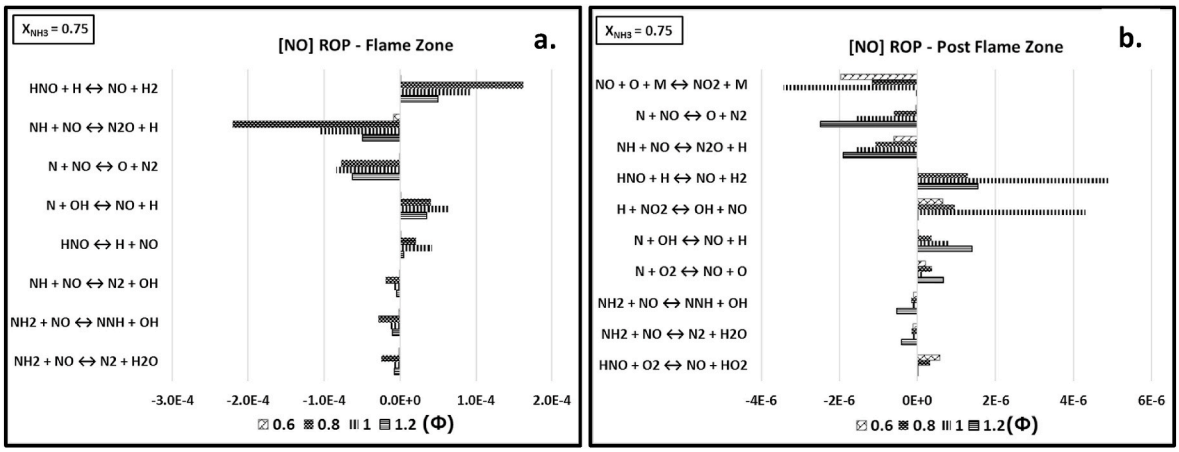

Fig. 12. Absolute and integrated ROPs of [NO] at the (a) flame zone [Unit – mole/cm^3-sec], and (b) post-flame zone [Unit – mole/cm^2-sec], respectively for X_{NH3} = 0.75 and changing Φ.

3.2. NO emissions

Fig. 10 plots the measured NO emissions at the exhaust for $0.75 \leq X_{NH3} \leq 1.00$ and $0.55 = \Phi \leq 1.3$. The solid line shows NO production predictions by the CRN network at $X_{NH3} = 0.75$. NO production at the exhaust for certain ranges of lean conditions across different blends could not be captured as the values exceeded the measurement range of the gas analyser. However, the predictions from the CRN network for $X_{NH3} = 0.75$ (blue solid line, Fig. 10) give an indication of NO emissions at these ranges, peaking at around $\Phi = 0.80$, a trend already seen in other works [20]. Measured NO emissions drop as X_{NH3} increases up to $\Phi > 1.1$, point at which NO emissions for the $75/25_{VOL.\%}$ blend drop nearly to zero. However, the other blends considered here still show some NO emissions until $\Phi = 1.3$, where they all drop to near zero.

Fig. 11 displays the normalized sensitivity coefficients for overall NO concentrations at the flame zone while Fig. 12 (a) and (b) show the absolute and integrated ROP of [NO] at the flame and post-flame zones, respectively, at $X_{NH3} = 0.75$ and changing Φ. From the ROP graphs, HNO is the main source of NO production at both flame and post flame zones through the reaction HNO + H ↔ NO + H_2 (R3). And from the sensitivity graph in Fig. 10, the major source of HNO production is identified as NH + OH ↔ HNO + H (R4). From Fig. 6(a), OH* and NH* productions were the highest at $\Phi = 0.8$, subsequently producing most NO. Also, from the first row of Figs. 4 and 5, NH* and NH_2* radicals distributions cover a larger area as Φ increases. As stated earlier, reaction R2 is responsible for producing important radicals which help oxidising ammonia, thus producing fuel NO through the route $NH_3 \rightarrow NH_2 \rightarrow NH \rightarrow HNO \rightarrow NO$. Reaction R2 displays negative sensitivity for NO at the rich condition due to unavailability of O_2. Therefore, from the sensitivity graph in Fig. 11, any reaction consuming OH and H radicals display negative sensitivity for [NO]. Other sources of NO are when atomic N reacts with OH radicals (extended Zeldovich) and through HNO dissociation reaction to NO and H radicals.

Further, NO converts to N_2O and N_2 by reacting with NH and molecular N, respectively. Also, the ROP of these two reactions are dependent on NO produced through reaction R3. As most NO was predicted to be produced at $\Phi = 0.8$, followed by 1.0, the overall ROPs for NO production are the highest at these two equivalence ratios. NO reduction to N_2O will be analysed at the latter part of this investigation. Fig. 6(b) shows increased NH_2* intensity with increasing Φ. NH_2 radicals are well documented for their de-NOxing characteristics through the chain branching reactions $NH_2 + NO \leftrightarrow NNH + OH$ (R5) and the chain terminating reaction $NH_2 + NO \leftrightarrow H_2O + N_2$ (R6) [48–51]. Also, these two reactions (R5 and R6) contribute mostly towards NO consumption at rich conditions, Fig. 12(b), a point reflected in the captured minimum NO emissions at $\Phi = 1.2$, Fig. 10.

Fig. 13 (a) and (b) show the normalized sensitivity coefficients and absolute ROP of [NO], respectively, at the flame zone for $\Phi = 0.65$ and changing X_{NH3}. With the availability of plenty of excess O_2 at very lean condition, HNO converts to NO by reacting with molecular O_2 (R5). Similarly, another significant source of NO is through the reaction N + $O_2 \leftrightarrow$ NO + O (Zeldovich, R6) at this lean condition. From Fig. 6(b), all the radicals (NH, OH and NH_2) decrease with increasing ammonia content. H, O and OH radicals production decreases with decreasing H_2

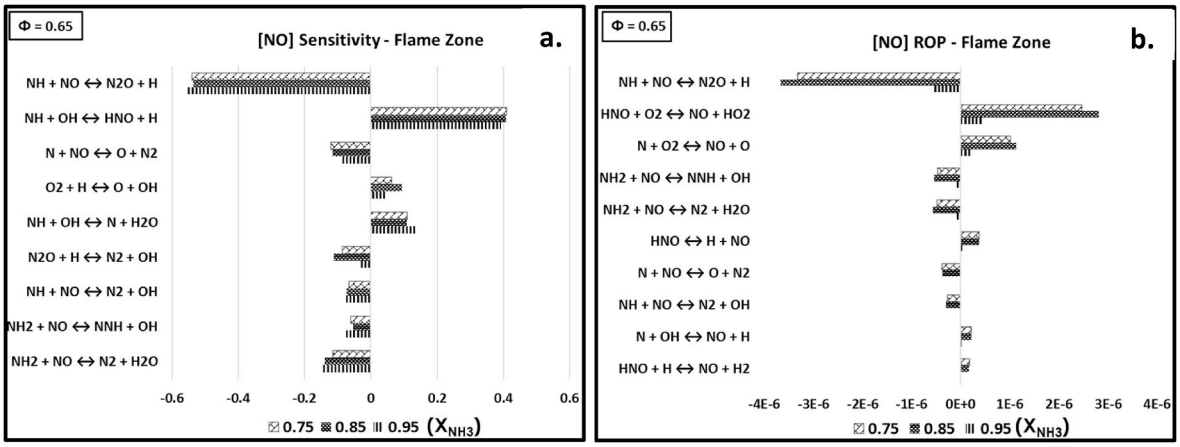

Fig. 13. (a) Normalized sensitivity coefficients and (b) Absolute ROP [Unit – mole/cm^3-sec] of [NO] at the flame zone for $\Phi = 0.65$ and changing X_{NH3}.

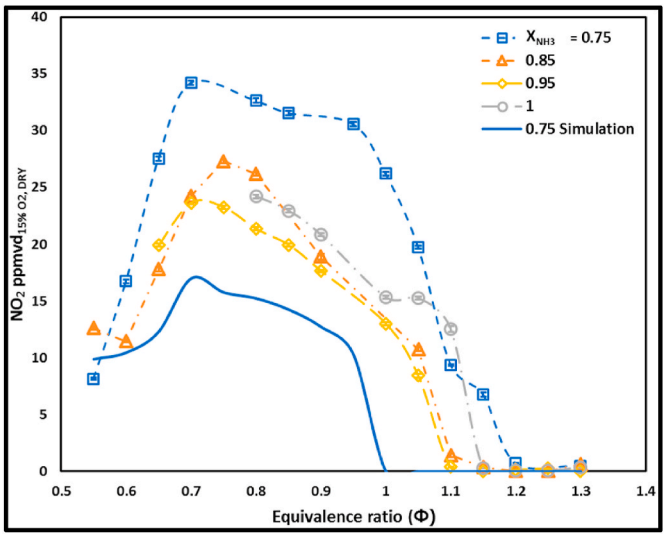

Fig. 14. Sampled NO_2 emissions for changing X_{NH3} and Φ. Markers show experimental results and the solid line shows simulation prediction.

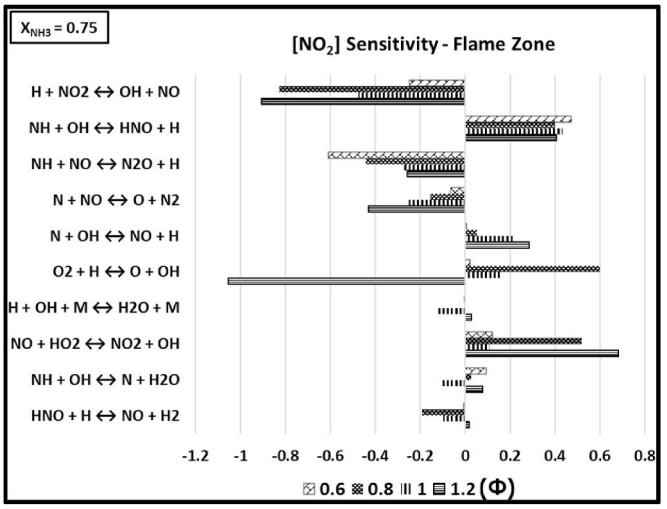

Fig. 15. Normalized sensitivity coefficients of [NO_2] at the flame zone for X_{NH3} = 0.75 and changing Φ.

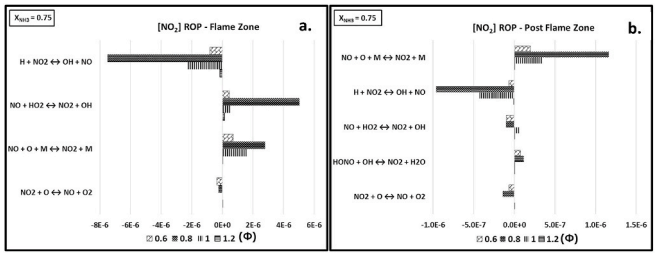

Fig. 16. Absolute and integrated ROP of [NO_2] at the (a) flame zone [Unit – mole/cm^3-sec], and (b) post-flame zone [Unit – mole/cm^2-sec] for X_{NH3} = 0.75 and changing Φ.

content in the blends, thereby affecting the productions of NH and NH_2 radicals as well, and thus reducing NO formation.

3.3. NO_2 emissions

Fig. 14 plots the measured NO emissions at the exhaust for 0.75 ≤ X_{NH3} ≤ 1.00 and 0.55 ≤ Φ ≤ 1.3. The solid line shows NO production predictions by the CRN network at X_{NH3} = 0.75. Even though the numerical predictions for NO_2 follow the experimental trends, they underpredict NO_2 by a substantial margin, another point of interest for modellers. Measured NO_2 peaks between 0.7 and 0.8 equivalence ratio for the blends considered here. Steep rise in NO_2 production was observed from the very lean conditions up to the peak production, followed by reduction as Φ increases, and finally dropping to zero at around Φ = 1.2. Fig. 15 displays the normalized sensitivity coefficients for overall NO_2 concentrations at the flame zone while Fig. 16 (a) and (b) show the absolute and integrated ROP of [NO_2] at the flame and post-flame zones, respectively, at X_{NH3} = 0.75 and changing Φ. NO mainly converts to NO_2 through two reactions at the flame zone: NO + HO_2 ↔ NO_2 + OH (R7), and the third body reaction NO + O + M ↔ NO_2 + M (R8). ROPs for both these reactions are substantially higher at Φ = 0.8, compared to other equivalence ratios considered here. This observation can be attributed to the increased availability of NO at Φ = 0.8. However, most of this NO_2 reacts with H and O radicals to revert to NO. From Fig. 16(b), reaction R8 is the most significant NO_2 production route at the post-flame zone. Recent study by Sabia et al. [52] concluded that ammonia can have high third body efficiency which has not been

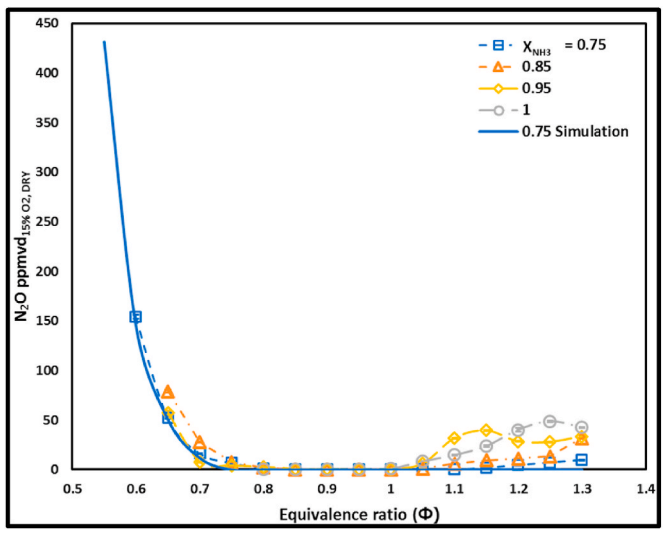

Fig. 17. Sampled N_2O emissions for changing X_{NH3} and Φ. Markers show experimental results and the solid line shows simulation prediction.

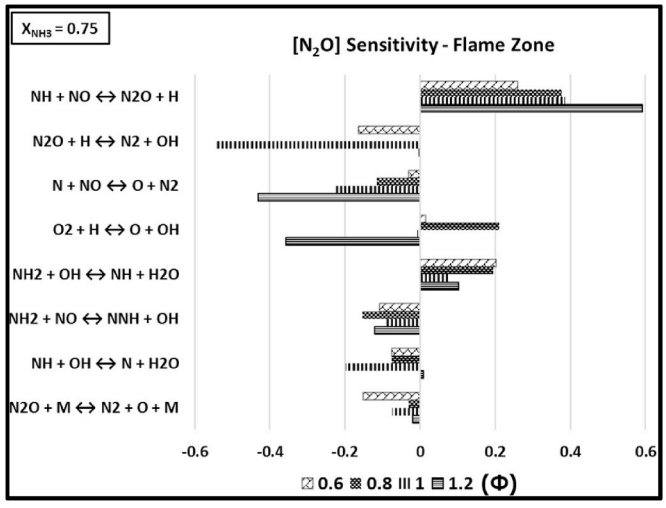

Fig. 18. Normalized sensitivity coefficients of [N_2O] at the flame zone for X_{NH3} = 0.75 and changing Φ.

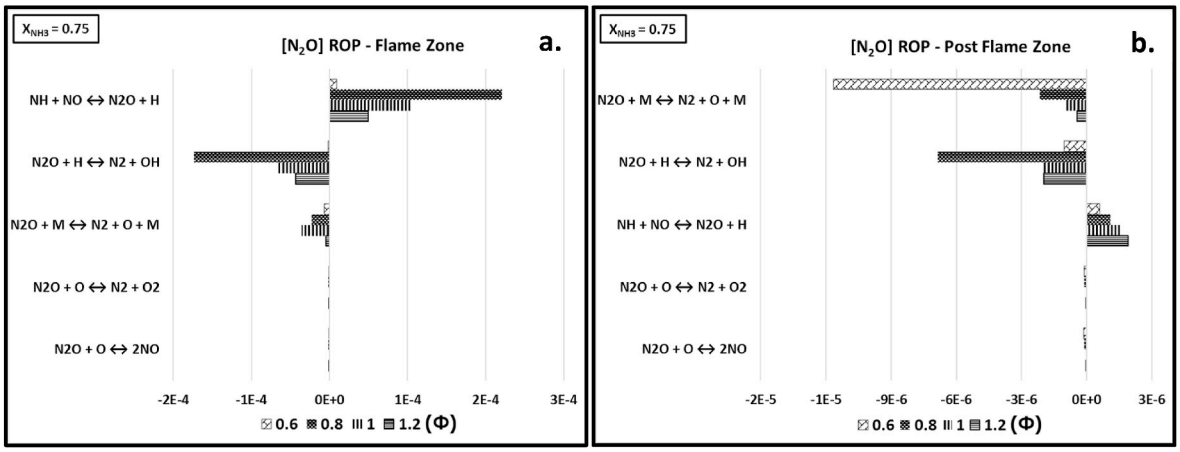

Fig. 19. Absolute and integrated ROP of [N_2O] at the (a) flame zone [Unit – mole/cm^3-sec], and (b) post-flame zone [Unit – mole/cm^2-sec] for $X_{NH3} = 0.75$ and changing Φ.

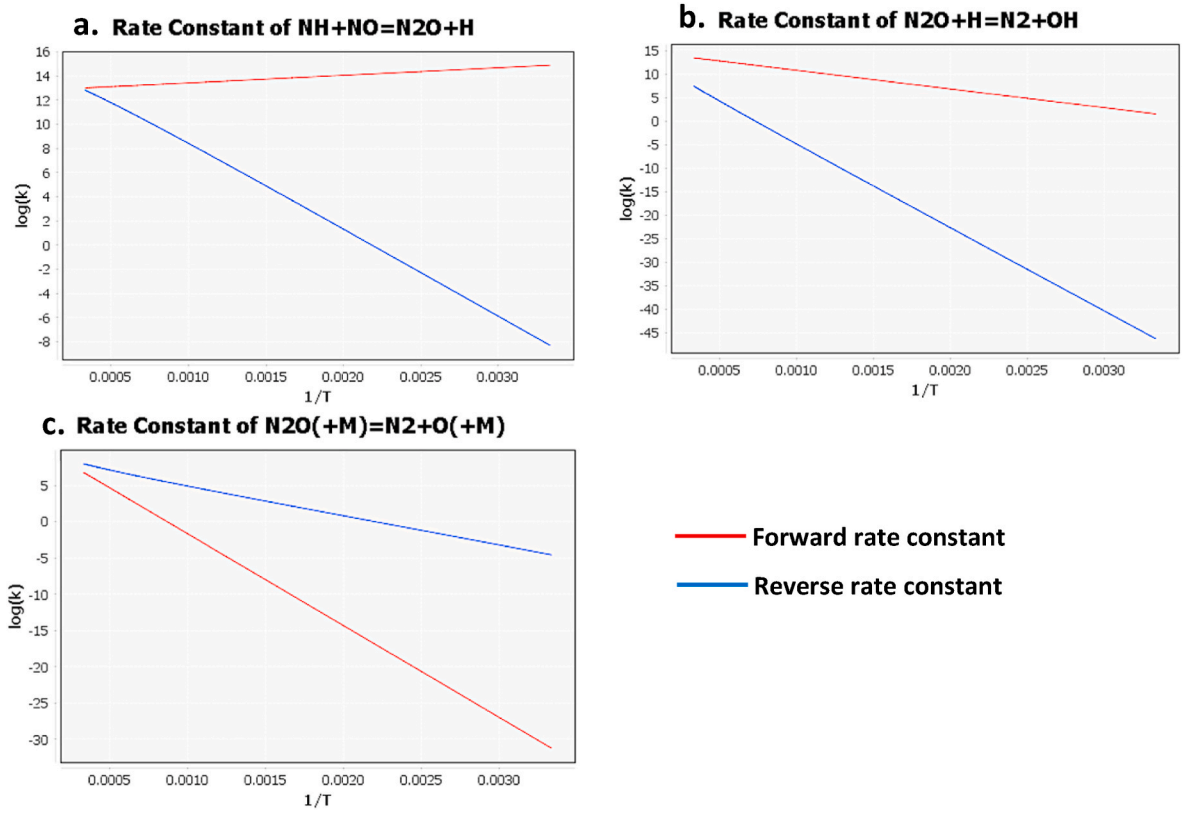

Fig. 20. Rate constants values for reactions (a) R9, (b) R10, and (c) R11.

considered in the ammonia oxidation kinetic mechanisms available in the literature yet. Consideration of this high third body efficiency can enhance the reaction rate of reaction R8 further and thus improve the model prediction of NO_2.

3.4. N_2O emissions

N_2O emissions measured at the exhaust for different ammonia/hydrogen blends and equivalence ratio are plotted in Fig. 17 which also shows the prediction by the CRN at $X_{NH3} = 0.75$ (blue solid line). Minimum N_2O productions were observed at $0.8 > \Phi > 1.0$ for all the blends considered here. However, N_2O productions at the lean conditions were more significant than the rich region. Numerical simulations at $X_{NH3} = 0.75$ were able to predict the emissions at the lean region but not so much for rich conditions. For the rich region, N_2O seems to keep increasing for $X_{NH3} = 0.75$ and 0.85, whereas N_2O emissions peak at $\Phi = 1.15$ and 1.25 for $X_{NH3} = 0.95$ and 1.0, respectively.

Fig. 18 displays the normalized sensitivity coefficients for overall N_2O concentrations at the flame zone while Fig. 19 (a) and (b) show the absolute and integrated ROPs of [N_2O] at flame and post-flame zones, respectively, at $X_{NH3} = 0.75$ and changing Φ. From Fig. 19, the main source of N_2O is from NO through the reaction $NH + NO \leftrightarrow N_2O + H$ (R9) and N_2O is reduced through the reactions: $N_2O + H \leftrightarrow N_2 + OH$ (R10) and $N_2O + M \leftrightarrow N_2 + O + M$ (R11). According to Stagni et al. [40], activation energy (E_A) values for reactions R9, R10 and R11 are −2893.9, 18,100 and 57,901, respectively. It must be noted R10 has a

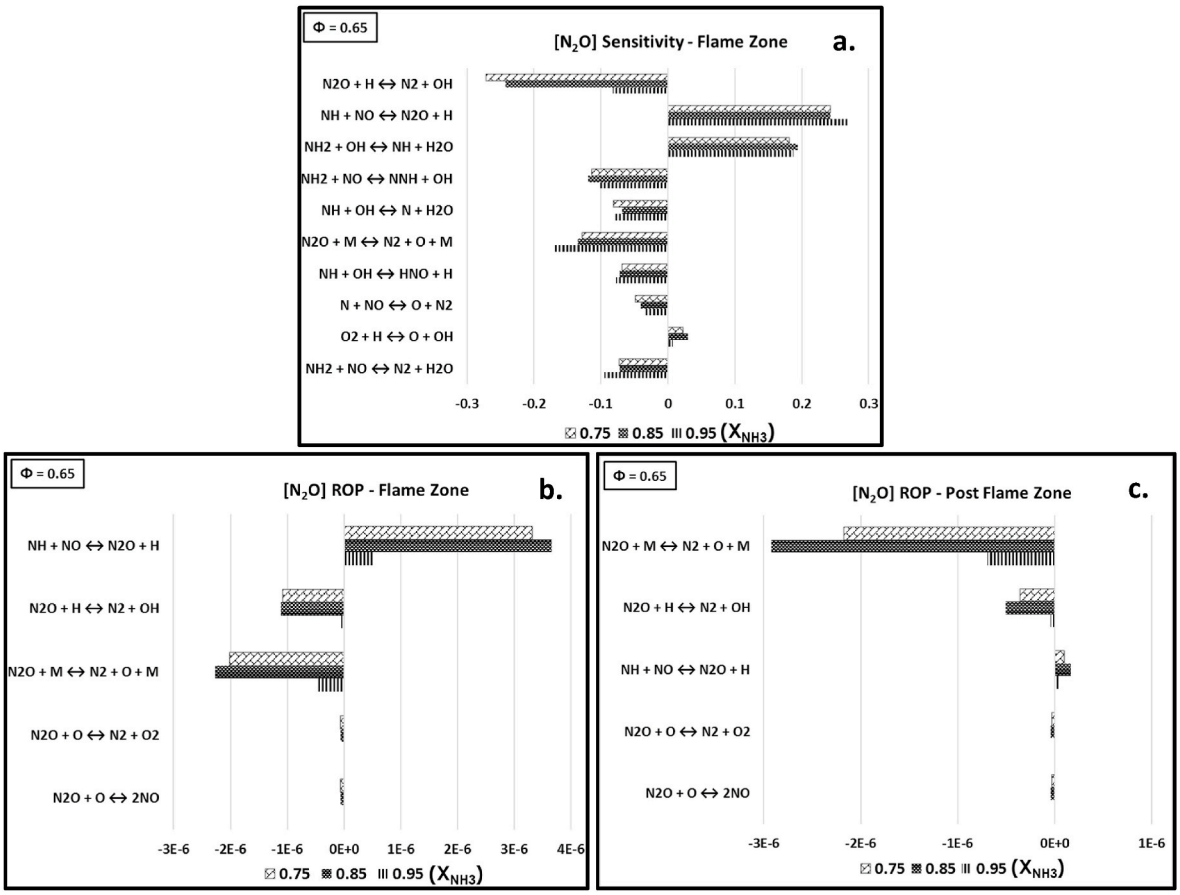

Fig. 21. (a) Normalized sensitivity coefficients (flame zone) and Absolute and integrated ROPs of [NO] at the (b) flame zone [Unit – mole/cm^3-sec], and (c) post-flame zone [Unit – mole/cm^2-sec], respectively for $\Phi = 0.65$ and changing X_{NH3}.

duplicated reaction in the mechanism with E_A of 4550. All the ROP diagrams with R10 show combined ROP values of the duplicated reactions. Reaction R11 is very sensitive to temperature due to its high activation energy requirements, whereas reaction R9 has the lowest temperature dependency among these three reactions. Fig. 20 shows the temperature dependency of these three reactions in terms of rate constant. At the flame zone, Fig. 19(a), N_2O formed rapidly at $\Phi = 0.8$, 1.0 and 1.2 in decreasing order via reaction R9. Further, the emission is mostly consumed through reaction R10 due to the presence of H radicals in the flame zone. This observation corresponds to the NH* intensity trend with changing Φ seen in Fig. 6(a). At the post-flame zone, Fig. 19 (b), more N_2O gets consumed, rather than produced, due to the decreased presence of H radicals across all equivalence ratios considered here. Due to the low reaction rates at $\Phi = 0.6$, it is hard to analyse N_2O formation/consumption and the impact of other reactions. Therefore, [N_2O] analysis has been carried out next for three blends ($X_{NH3} = 0.75$, 0.85, 0.95) at $\Phi = 0.65$. This slightly higher Φ is chosen due to stable flames where experimental data were taken.

From Fig. 6(b), NH* decreases with increasing ammonia content in the fuel mixtures and thus limits the NO conversion to N_2O via reaction R9. According to Nakamura and Shindo [53], with the increasing ammonia content in the fuel blends, ammonia chemistry plays the dominant role in flame chemistry and becomes more sensitive to heat losses. As reaction R11 is very sensitive to temperature, N_2O consumption reduces at the flame due to reduced temperature. Chemical time scale increases relative to the fuel residence time with increasing ammonia content in the fuel, thus contributing to reduced N_2O production as flame changes from 85% to 95% ammonia content. Fig. 21 (a) and (b) show the normalized sensitivity coefficients and absolute ROP of [NO], respectively, at the flame zone, and (c) shows integrated ROP at the post-flame zone for $\Phi = 0.65$ and changing X_{NH3}. From the sensitivity graph, influence of reaction R10 decreases with increasing X_{NH3} due to reduced availability of H radicals, whereas sensitivity to reaction R11 increases due to reduced flame temperature at high ammonia contents. From the ROP graphs at the flame and post-flame zones, Fig. 21 (b) and (c), N_2O production rate via reaction R9 reduces significantly at $X_{NH3} = 0.95$, reaffirming the observations earlier. Relative ROPs for reaction R11 increases compared to reaction R9 at the post-flame zone, thus N_2O is being reduced considerably at the post-flame zone. Similarly, observed N_2O emissions at rich conditions can also be attributed to decrease in flame temperature.

4. Conclusions

Different NH_3/H_2 blends were analysed at a range of equivalence ratios for a constant thermal power of 8 kW using a generic industrial scale swirl burner with a combination of exhaust emissions measurements, spatially resolved NH* and NH_2* chemiluminescence, spectrometry analyses and numerical simulations with Chemkin-Pro employing Stagni's mechanism.

Ammonia emissions captured at very lean conditions were attributed to flame instability, whereas unavailability of oxygen at the rich conditions contribute towards ammonia slip. Oxidation of ammonia was found to be dependent on OH radicals availability, thus highly dependent on the reaction $O_2 + H \leftrightarrow O + OH$.

NO emissions increased initially with increasing equivalence ratio, peaking around $\Phi = 0.8$ and then being reduced significantly to nearly zero at rich conditions. HNO was identified as the main contributor of fuel NO formation, whereas NO was found to be reduced to N_2O, NO_2 and N_2 by reacting with NH, HO_2 and atomic N, respectively. NO

production reduces with increasing ammonia mol fraction due to decrease in H, O and OH radicals' availability.

Similar to NO emissions, NO_2 emissions also peak between 0.7 and 0.8 equivalence ratio for the blends considered here. A $75/25_{VOL.\%}$ NH_3/H_2 blend was found to be producing considerable quantities of NO_2, whereas a $95/05_{VOL.\%}$ NH_3/H_2 blend had less NO_2 emissions. Most of the NO_2 converts back to NO by reacting with H radicals. N_2O emissions were the highest at very lean conditions and some emissions were also observed at rich regions. These emissions were attributed to low flame temperatures at those conditions. Considerable amount of N_2O revert to NO at the flame zone by reacting with H radicals. The third body reaction $N_2O + M \leftrightarrow N_2 + O + M$ was found to be very sensitive to temperature and was identified as the reason for reduced conversion of N_2O to NO at comparatively lower flame temperatures.

Finally, it was noted that there are still discrepancies between experiments and models, especially when it comes to boundary conditions of stability (very rich and very lean) for species such as ammonia and NO_2, topic of interest for further research.

Credit author statement

Syed Mashruk: Conceptualization, Methodology, Investigation, Software, Validation, Data curation, Writing-Original draft preparation. **Marina Kovaleva**: Software, Validation, Writing-Original draft preparation. **Ali Alnasif**: Software, Validation. **Cheng Tung Chong**: Writing – Review & Editing. **Akihiro Hayakawa**: Writing – Review & Editing. **Ekenechukwu C. Okafor**: Writing – Review & Editing. **Agustin Valera-Medina**: Conceptualization, Methodology, Resources, Visualization, Supervision, Writing – Review & Editing, Project administration, Funding acquisition.

Declaration of competing interest

The authors declare that they have no known competing financial interests or personal relationships that could have appeared to influence the work reported in this paper.

Data availability

DOI will be added in the Acknowledgement section.

Acknowledgements

This work was supported by the SAFE-AGT pilot (no. EP/T009314/1) with funding from the Engineering and Physical Sciences Research Council (EPSRC). The research was undertaken at Cardiff University's Thermofluids Lab (W/0.07) with invaluable technical support from Mr. Malcolm Seaborne. Information on the data underpinning the results presented here, including how to access them, can be found in the Cardiff University data catalogue at http://doi.org/10.17035/d.2022.0217184646.

Appendix A. Supplementary data

Supplementary data to this article can be found online at https://doi.org/10.1016/j.energy.2022.125183.

References

[1] Kurata O, Iki N, Matsunuma T, Inoue T, Tsujimura T, Furutani H, Kobayashi H, Hayakawa A. Performances and emission characteristics of NH3–air and NH3CH4–air combustion gas-turbine power generations. Proc Combust Inst 2017;36:3351–9. https://doi.org/10.1016/j.proci.2016.07.088.

[2] Valera-Medina A, Amer-Hatem F, Azad AK, Dedoussi IC, de Joannon M, Fernandes RX, Glarborg P, Hashemi H, He X, Mashruk S, McGowan J, Mounaim-Rouselle C, Ortiz-Prado A, Ortiz-Valera A, Rossetti I, Shu B, Yehia M, Xiao H, Costa M. Review on ammonia as a potential fuel: from synthesis to economics. Energy Fuel 2021;35:6964–7029. https://doi.org/10.1021/acs.energyfuels.0c03685.

[3] Elishav O, Mosevitzky Lis B, Miller EM, Arent DJ, Valera-Medina A, Grinberg Dana A, Shter GE, Grader GS. Progress and prospective of nitrogen-based alternative fuels. Chem Rev 2020;120:5352–436. https://doi.org/10.1021/acs.chemrev.9b00538.

[4] Kobayashi H, Hayakawa A, Somarathne KDKA, Okafor EC. Science and technology of ammonia combustion. Proc Combust Inst 2019;37:109–33. https://doi.org/10.1016/j.proci.2018.09.029.

[5] Verkamp FJ, Hardin MC, Williams JR. Ammonia combustion properties and performance in gas-turbine burners. In: Symposium (International) on combustion; 1967. p. 985–92.

[6] Lhuillier C, Brequigny P, Lamoureux N, Contino F, Mounaïm-Rousselle C. Experimental investigation on laminar burning velocities of ammonia/hydrogen/air mixtures at elevated temperatures. Fuel 2020;263:116653. https://doi.org/10.1016/j.fuel.2019.116653.

[7] Hayakawa A, Goto T, Mimoto R, Kudo T, Kobayashi H. NO formation/reduction mechanisms of ammonia/air premixed flames at various equivalence ratios and pressures. Mech Eng J 2015;2. https://doi.org/10.1299/mej.14-00402. 14-00402-14–00402.

[8] Khateeb AA, Guiberti TF, Zhu X, Younes M, Jamal A, Roberts WL. Stability limits and NO emissions of technically-premixed ammonia-hydrogen-nitrogen-air swirl flames. Int J Hydrogen Energy 2020;45:22008–18. https://doi.org/10.1016/j.ijhydene.2020.05.236.

[9] Mei B, Zhang X, Ma S, Cui M, Guo H, Cao Z, Li Y. Experimental and kinetic modeling investigation on the laminar flame propagation of ammonia under oxygen enrichment and elevated pressure conditions. Combust Flame 2019;210:236–46. https://doi.org/10.1016/j.combustflame.2019.08.033.

[10] Mei B, Ma S, Zhang Y, Zhang X, Li W, Li Y. Exploration on laminar flame propagation of ammonia and syngas mixtures up to 10 atm. Combust Flame 2020;220:368–77. https://doi.org/10.1016/j.combustflame.2020.07.011.

[11] Okafor EC, Naito Y, Colson S, Ichikawa A, Kudo T, Hayakawa A, Kobayashi H. Experimental and numerical study of the laminar burning velocity of CH4–NH3–air premixed flames. Combust Flame 2018;187:185–98. https://doi.org/10.1016/j.combustflame.2017.09.002.

[12] Mashruk S, Xiao H, Pugh D, Chiong MC, Runyon J, Goktepe B, Giles A, Valera-Medina A. Numerical analysis on the evolution of NH2 in ammonia/hydrogen swirling flames and detailed sensitivity analysis under elevated conditions. Combust Sci Technol 2021:1–28. https://doi.org/10.1080/00102202.2021.1990897.

[13] Mashruk S, Vigueras-Zuniga MO, Tejeda-del-Cueto ME, Xiao H, Yu C, Maas U, Valera-Medina A. Combustion features of CH4/NH3/H2 ternary blends. Int J Hydrogen Energy 2022. https://doi.org/10.1016/J.IJHYDENE.2022.03.254.

[14] Comotti M, Frigo S. Hydrogen generation system for ammonia–hydrogen fuelled internal combustion engines. Int J Hydrogen Energy 2015;40:10673–86. https://doi.org/10.1016/j.ijhydene.2015.06.080.

[15] The Royal Society. Ammonia: zero-carbon fertiliser, fuel and energy store. Policy Briefing; 2020. 2020.

[16] Pugh D, Bowen P, Valera-Medina A, Giles A, Runyon J, Marsh R. Influence of steam addition and elevated ambient conditions on NO x reduction in a staged premixed swirling NH 3/H 2 flame. Proc Combust Inst 2019;37:5401–9. https://doi.org/10.1016/j.proci.2018.07.091.

[17] Zhang M, An Z, Wang L, Wei X, Jianayihan B, Wang J, Huang Z, Tan H. The regulation effect of methane and hydrogen on the emission characteristics of ammonia/air combustion in a model combustor. Int J Hydrogen Energy 2021;46:21013–25. https://doi.org/10.1016/J.IJHYDENE.2021.03.210.

[18] Franco MC, Rocha RC, Costa M, Yehia M. Characteristics of NH3/H2/air flames in a combustor fired by a swirl and bluff-body stabilized burner. Proc Combust Inst 2020;38. https://doi.org/10.1016/j.proci.2020.06.141.

[19] Valera-Medina A, Marsh R, Runyon J, Pugh D, Beasley P, Hughes T, Bowen P. Ammonia–methane combustion in tangential swirl burners for gas turbine power generation. Appl Energy 2017;185:1362–71. https://doi.org/10.1016/j.apenergy.2016.02.073.

[20] Valera-Medina A, Pugh DG, Marsh P, Bulat G, Bowen P. Preliminary study on lean premixed combustion of ammonia-hydrogen for swirling gas turbine combustors. Int J Hydrogen Energy 2017;42:24495–503.

[21] Sorrentino G, Sabia P, Bozza P, Ragucci R, de Joannon M. Low-NOx conversion of pure ammonia in a cyclonic burner under locally diluted and preheated conditions. Appl Energy 2019;254:113676. https://doi.org/10.1016/j.apenergy.2019.113676.

[22] Ariemma GB, Sabia P, Sorrentino G, Bozza P, de Joannon M, Ragucci R. Influence of water addition on MILD ammonia combustion performances and emissions. Proc Combust Inst 2020;38(4):5147–54. https://doi.org/10.1016/j.proci.2020.06.143.

[23] Okafor EC, Somarathne KDKA, Hayakawa A, Kudo T, Kurata O, Iki N, Kobayashi H. Towards the development of an efficient low-NOx ammonia combustor for a micro gas turbine. Proc Combust Inst 2019;37:4597–606. https://doi.org/10.1016/j.proci.2018.07.083.

[24] Okafor EC, Somarathne KDKA, Ratthanan R, Hayakawa A, Kudo T, Kurata O, Iki N, Tsujimura T, Furutani H, Kobayashi H. Control of NOx and other emissions in micro gas turbine combustors fuelled with mixtures of methane and ammonia. Combust Flame 2020;211:406–16. https://doi.org/10.1016/j.combustflame.2019.10.012.

[25] Okafor EC, Kurata O, Yamashita H, Inoue T, Tsujimura T, Iki N, Hayakawa A, Ito S, Uchida M, Kobayashi H. Liquid ammonia spray combustion in two-stage micro gas turbine combustors at 0.25 MPa; Relevance of combustion enhancement to flame stability and NOx control. Appl Energy Combust Sci 2021;7:100038. https://doi.org/10.1016/j.jaecs.2021.100038.

[26] Guteša Božo M, Mashruk S, Zitouni S, Valera-Medina A. Humidified ammonia/hydrogen RQL combustion in a trigeneration gas turbine cycle. Energy Convers Manag 2021;227:113625. https://doi.org/10.1016/j.enconman.2020.113625.
[27] Zhu X, Khateeb AA, Guiberti TF, Roberts WL. NO and OH* emission characteristics of very-lean to stoichiometric ammonia–hydrogen–air swirl flames. Proc Combust Inst 2021;38:5155–62. https://doi.org/10.1016/j.proci.2020.06.275.
[28] Global Warming Potentials (IPCC Second Assessment Report) | UNFCCC, https://unfccc.int/process/transparency-and-reporting/greenhouse-gas-data/greenhouse-gas-data-unfccc/global-warming-potentials Last accessed: 19 August 2022.
[29] Lee JH, Kim JH, Park JH, Kwon OC. Studies on properties of laminar premixed hydrogen-added ammonia/air flames for hydrogen production. Int J Hydrogen Energy 2010;35:1054–64. https://doi.org/10.1016/j.ijhydene.2009.11.071.
[30] Okafor EC, Tsukamoto M, Hayakawa A, Somarathne KA, Kudo T, Tsujimura T, Kobayashi H. Influence of wall heat loss on the emission characteristics of premixed ammonia-air swirling flames interacting with the combustor wall. Proc Combust Inst 2021;38:5139–46. https://doi.org/10.1016/J.PROCI.2020.06.142.
[31] Ferrarotti M, Bertolino A, Amaduzzi R, Parente A. On the influence of kinetic uncertainties on the accuracy of numerical modeling of an industrial flameless furnace fired with NH3/H2 blends: a numerical and experimental study. Front Energy Res 2020;8:1–15. https://doi.org/10.3389/fenrg.2020.597655.
[32] Otomo J, Koshi M, Mitsumori T, Iwasaki H, Yamada K. Chemical kinetic modeling of ammonia oxidation with improved reaction mechanism for ammonia/air and ammonia/hydrogen/air combustion. Int J Hydrogen Energy 2018;43(5):3004–14. https://doi.org/10.1016/j.ijhydene.2017.12.066.
[33] Mei B, Zhang J, Shi X, Xi Z, Li Y. Enhancement of ammonia combustion with partial fuel cracking strategy: laminar flame propagation and kinetic modeling investigation of NH3/H2/N2/air mixtures up to 10 atm. Combust Flame 2021;231:111472. https://doi.org/10.1016/j.combustflame.2021.111472.
[34] Mashruk S, Kovaleva M, Chong CT, Hayakawa A, Okafor E, Valera-Medina A. Nitrogen oxides as a by-product of ammonia/hydrogen combustion regimes. Chem Eng Trans 2021;89:613–8. https://doi.org/10.3303/CET2189103.
[35] Schott GL, Blair LS, Jr., J.D.M.. Exploratory shock-wave study of thermal nitrogen trifluoride decomposition and reactions of nitrogen trifluoride and dinitrogen tetrafluoride with hydrogen. J Phys Chem 2002;77:2823–30. https://doi.org/10.1021/J100642A001.
[36] Liu Y, Sun X, Sethi V, Nalianda D, Li YG, Wang L. Review of modern low emissions combustion technologies for aero gas turbine engines. 2017.
[37] Mashruk S. NO formation analysis using chemical reactor modelling and LIF measurements on industrial swirl flames. 2020. PhD Thesis, https://orca.cf.ac.uk/136590/1/2020MashrukSPhD.pdf.
[38] Shaddix CR. In: 10th US, editor. A new method to compute the proper radiant heat transfer correction of bare-wire thermocouple measurements. National Combustion Meeting; 2017.
[39] British standard: BS 1SO 11042-1:1996. Gas Turbines-Exhaust Gas Emission; 1996.
[40] Stagni Alessandro, Cavallotti Carlo, Arunthanayothin Suphaporn, Song Yu, Herbinet Olivier, Battin-Leclerc Frédérique, Faravelli Tiziano. An experimental, theoretical and kinetic-modeling study of the gas-phase oxidation of ammonia. React Chem Eng 2020;5:696–711. https://doi.org/10.1039/C9RE00429G.
[41] Zitouni S-E, Mashruk S, Mukundakumar N, Brequigny P, Zayoud A, Pucci E, Macchiavello S, Contino F, Mounaim-Rousselle C, Bastiaans R, Valera-Medina A. Ammonia blended fuels-energy solutions for a green future. In: Gas turbines in a carbon-neutral society, 10th International gas turbine conference; 2021.
[42] d'Agostino R, Cramarossa F, De Benedictis S, Ferraro G. Kinetic and spectroscopic analysis of NH3 decomposition under R.F. Plasma at moderate pressures. Plasma Chem Plasma Process 1981;1:19–35. https://doi.org/10.1007/BF00566373.
[43] Pugh D, Runyon J, Bowen P, Giles A, Valera-Medina A, Marsh R, Goktepe B, Hewlett S. An investigation of ammonia primary flame combustor concepts for emissions reduction with OH*, NH2* and NH* chemiluminescence at elevated conditions. Proc Combust Inst 2021;38:6451–9. https://doi.org/10.1016/j.proci.2020.06.310.
[44] Roose TR, Hanson RK, Kruger CH. A shock tube study of the decomposition of no in the presence of NH3. Symp Combust 1981;18:853–62. https://doi.org/10.1016/S0082-0784(81)80089-6.
[45] Ballester J, García-Armingol T. Diagnostic techniques for the monitoring and control of practical flames. Prog Energy Combust Sci 2010;36:375–411. https://doi.org/10.1016/j.pecs.2009.11.005.
[46] Sheehe SL, Jackson SI. Spatial distribution of spectrally emitting species in a nitromethane–air diffusion flame and comparison with kinetic models. Combust Flame 2020;213:184–93. https://doi.org/10.1016/J.COMBUSTFLAME.2019.10.026.
[47] Manna MV, Sabia P, Sorrentino G, Viola T, Ragucci R, de Joannon M. New insight into NH3-H2 mutual inhibiting effects and dynamic regimes at low-intermediate temperatures. Combust Flame 2022;111957. https://doi.org/10.1016/J.COMBUSTFLAME.2021.111957.
[48] Mashruk S, Xiao H, Valera-Medina A. Rich-Quench-Lean model comparison for the clean use of humidified ammonia/hydrogen combustion systems. Int J Hydrogen Energy 2020;46:4472–84. https://doi.org/10.1016/j.ijhydene.2020.10.204.
[49] Pugh D, Bowen P, Valera-Medina A, Giles A, Runyon J, Marsh R. Influence of steam addition and elevated ambient conditions on NOx reduction in a staged premixed swirling NH3/H2 flame. Proc Combust Inst 2019;37:5401–9. https://doi.org/10.1016/j.proci.2018.07.091.
[50] Rahinov I, Ditzian N, Cheskis S. NH2 radical formation by ammonia pyrolysis in a temperature range of 800–1000 K. 2003 Appl Phys B 2003;775(77):541–6. https://doi.org/10.1007/S00340-003-1267-7.
[51] Zhou Q, Yao SC, Russell A, Boyle J. Flue Gas NOX Reduction Using Ammonia Radical Injection 2012;42:1193–7. https://doi.org/10.1080/10473289.1992.10467067. https://doi.org/10.1080/10473289.1992.10467067.
[52] Sabia P, Manna MV, Ragucci R, de Joannon M. Mutual inhibition effect of hydrogen and ammonia in oxidation processes and the role of ammonia as "strong" collider in third-molecular reactions. Int J Hydrogen Energy 2020;45:32113–27. https://doi.org/10.1016/j.ijhydene.2020.08.218.
[53] Nakamura H, Shindo M. Effects of radiation heat loss on laminar premixed ammonia/air flames. Proc Combust Inst 2019;37:1741–8. https://doi.org/10.1016/J.PROCI.2018.06.138.